PERGAMON

Available online at www.sciencedirect.com

SCIENCE DIRECT®

Computers & Fluids 32 (2003) 1473–1495

computers & fluids

www.elsevier.com/locate/compfluid

# An adaptive shock-capturing algorithm for solving unsteady reactive flows

G. Billet [a,*], R. Abgrall [b]

[a] *ONERA BP 72-29, av. de la Division Leclerc, 92322 Châtillon Cedex, France*

[b] *Institut Universitaire de France et Université de Bordeaux, 351 cours de la Libération, 33405 Talence, France*

Received 26 September 2001; received in revised form 2 July 2002; accepted 18 October 2002

**Abstract**

A new double flux model is associated with the recent MUSCL-AUSM$^+$-triad approach. This coupling allows to do rapid, accurate and stable numerical computations. 1-D and 2-D inert and reactive flows are presented.



*Keywords:* MUSCL approach; TVD schemes; Euler and Navier–Stokes equations; Reactive flows

## 1. Introduction

The simulation of unsteady flows where very stiff phenomena occur, requires that the algorithms have some qualities. Particularly, when several reactive species are present in the flow, the strong gradients appearing across the flame have to be captured properly. It is necessary to use a method that is able to follow the physical and chemical events with good accuracy and stability if the wavelike oscillatory behavior have to be taken into account. This accuracy is also linked with the mesh refinement and consequently with the number of grid points, therefore the approach has to be easily vectorizable, parallelizable and to have a number of elementary operations as small as possible in order to have reasonable computational costs. At the end, if shock waves exist in the flow or may be formed, it is judicious to apply a 'shock capturing scheme'. In order to satisfy all these constraints, the approach presented in [1,2] has been retained. It uses a triad of limiters that minimizes the numerical error terms while keeping the stability and robustness of the well-known TVD-MUSCL schemes.

* Corresponding author. Fax: +33-1467-34266.
*E-mail address:* billet@onera.fr (G. Billet).

0045-7930/03/$ - see front matter 
doi:10.1016/S0045-7930(03)00004-5

When several species diffuse through an interface where the pressure and velocity are constant, the resolution of the hyperbolic part of the Navier–Stokes equations in conservative form develops pressure oscillations at the interface [3]. Some models have been proposed to simulate multi-component flows but either they present others inconveniences as the appearance of oscillations on others quantities [3–5], either they are written for specific cases as the tracking of material fronts without mixing [6,7], or for studies of species mixing with constant $C_{Pi}$ [8]. The cancellation of pressure oscillations is possible only if the primitive algorithm is not strictly conservative [9,10].

Recently, a simple model called 'double flux model' preserving the pressure and the velocity across the contact discontinuities has been presented [11]. We show that this model can be extended to the reactive flows composed with species whose $C_{Pi}$ depend on the temperature. This model is coupled with the recent *AUSM*$^+$*-MUSCL-triad* approach [1,2]. Its implementation is easy and the computational cost is cheap. We have focused our attention on the hyperbolic terms of the Navier–Stokes equations. The diffusion terms, when they are called, are solved with classical second-order centered schemes. This 'double flux model' is applied to 1-D and 2-D $H_2$–$O_2$ and $H_2$–$O_2$–$N_2$ front flames with the Rogers–Chinitz combustion model [12]. Firstly, by comparison with DNS results obtained from a code developed by D. Thévenin et al. [13], we show that the used numerical approach has a negligible numerical diffusion and captures correctly the convection of a front between two different gases. After that, we apply this model to a 1-D and a circular $H_2$–$O_2$ reactive front. The pressure and velocity are effectively preserved. At the end, the interaction vortices-front flames is studied. The vortex pair is created by the interaction between a spot of temperature and a shock. The set up of the turbulence field comes from the oscillation of the shock and the development of a pressure field after this interaction emphasized by the periodic conditions in the transverse direction. Two front flames are located just behind the shock. The distortion of the flames, first by the vortices and after that by the turbulent field, is studied.

## 2. Equations, models and numerical algorithms

### 2.1. Equations

The basic equations studied in this paper come from the hyperbolic part of the compressible Navier–Stokes equations applied on a reactive multi-component mixture. The 1-D conservative form is written:

$$\begin{aligned} &V_t + f_x = S \quad \text{with} \\ &V = \begin{bmatrix} \rho Y_i \\ \rho u \\ \rho E \end{bmatrix}, \quad f = \begin{bmatrix} \rho u Y_i \\ \rho u^2 + p \\ \rho u H \end{bmatrix}, \quad S = \begin{bmatrix} \overset{\circ}{W}_i \\ 0 \\ 0 \end{bmatrix} \\ &V(x,0) = V^0(x), \quad -\infty < x < +\infty, \quad t \geqslant 0. \end{aligned} \tag{1}$$

$\rho$, $Y_i$, $u$, $p$, $T$, $E$ and $H$ represent the density, the mass fraction of species $i$, the velocity, the static pressure, the temperature, the total energy and the total enthalpy. To close this system, the

equation of state, the total energy, the specific heat at constant pressure and the relation for the sum of the species mass fractions are given by:

$$\begin{aligned} p &= \rho \Re T \sum_{i=1}^{N} \frac{Y_i}{M_i}, \\ E &= \sum_{i=1}^{N} \left( h_{i0} Y_i + \int_{T_0}^{T} Y_i C_{Pi}(s)\,\mathrm{d}s \right) - \frac{p}{\rho} + \frac{u^2}{2}, \\ C_P &= \sum_{i=1}^{N} Y_i C_{Pi}, \quad \sum_{i=1}^{N} Y_i = 1, \quad C_{Pi} = C_{Pi}(T), \end{aligned} \tag{2}$$

where $h_{i0}$ and $T_0$ are the heat and temperature formations for species $i$, $M_i$ and $C_{Pi}$ the molecular weight and specific heat at constant pressure of species $i$ and $\Re$ the universal gas constant. $\mathring{W}_i$ represent the chemical reaction rates.

Each $C_{Pi}$ is determined by a continuous piecewise linear function in temperature based on JANNAF tables:

$$C_{Pi} = a_i^k T + b_i^k$$

with $a_i^k$ and $b_i^k$ constants on the interval of temperature $I_k = [(k-1)T^\Delta, kT^\Delta]$, $k = 1, 2, 3, \ldots$ and $T^\Delta = 100$ K. When $T \in I_m$, enthalpy $h_i$ is expressed

$$h_i = h_{i0} + \sum_{k=1}^{m} \int_{T_{k-1}}^{T_k} (a_i^k s + b_i^k)\,\mathrm{d}s + \int_{T_m}^{T} (a_i^m s + b_i^m)\,\mathrm{d}s = h_{i0}^{m'} + \int_{T_m}^{T} (a_i^m s + b_i^m)\,\mathrm{d}s.$$

In the last interval $I_m$, the linear evolution of $C_{Pi}$ is replaced by a constant evolution $C_{Pi} = \overline{b_i^m}$. So as to keep the correct value of $h_i$, the expression of $\overline{b_i^m}$ is

$$\overline{b_i^m} = \frac{a_i^m}{2}(T + T_m) + b_i^m.$$

Writing $h_{i0}^m = h_{i0}^{m'} - \overline{b_i^m} T_m$ and $h_0^m = \sum_{i=1}^{N} h_{i0}^m Y_i$, $E$ is expressed

$$E = h_0^m + \sum_{i=1}^{N} \overline{b_i^m} Y_i T - \frac{p}{\rho} + \frac{u^2}{2} = h_0^m + C_P T - \frac{p}{\rho} + \frac{u^2}{2} = h_0^m + \frac{p}{\rho(\gamma - 1)} + \frac{u^2}{2}. \tag{3}$$

We know Eq. (1) are ill-adapted to solve the material fronts separating two fluids having different values of the ratio of the specific heat $\gamma$ (see [3,9,10]). The 'double flux model' allows to cure this weakness. We extend this model to flows when $\gamma$ depends on the species but on the temperature too.

### 2.2. Double flux model

When $u$ ($u \neq 0$) and $p$ are constant at time $n$, the continuity and momentum equations give

$$\begin{aligned} \delta\rho &= -\sigma u \Delta\rho, \\ \delta(\rho u) &= -\sigma u^2 \Delta\rho, \end{aligned} \tag{4}$$

where $\sigma = \delta t / \Delta x$, $\Delta(\bullet) = (\bullet)_{j+1/2}^n - (\bullet)_{j-1/2}^n$ and $\delta(\bullet) = (\bullet)_j^{n+1} - (\bullet)_j^n$.

And therefore

$$u^{n+1} = u^n.$$

The velocity is conserved.

The energy equation is reduced, from relations (3) and (4), to

$$\delta(\rho h_0^m) + p\delta\left(\frac{1}{\gamma-1}\right) + \frac{1}{\gamma-1}\delta p = -\sigma u\left[\Delta(\rho h_0^m) + p\Delta\left(\frac{\gamma}{\gamma-1}\right)\right].$$

The pressure is conserved ($\delta p = 0$) if $\gamma$ and $\rho h_0^m$ are frozen on the domain $[j-1/2, j+1/2]\times[n, n+1]$. The principle of the 'double flux model' is based on this result and includes two steps. The first step uses the previous result to keep a uniform pressure across the interface and the second step modifies the thermodynamical values, that have been frozen during the first step, in order to obtain the correct value of the total energy. This model can be applied to the finite thickness interfaces as the diffusion zones where $\gamma$ varies not only with the species concentration but with the temperature variations too.

The construction proposed, taken from [10], holds for all numerical schemes that satisfy

$$\text{if } u_j^n \text{ and } p_j^n \text{ are uniform, then } u_j^{n+1} = u_j^n.$$

Flux splitting schemes, such as *van Leer* or $AUSM$ do not. $AUSM^+$ fulfills this constraint thanks to the concept of the common speed of sound [15,16].

### 2.2.1. First step

In the $MUSCL$ approach, the interface flux is classically expressed

$$F_{j+\frac{1}{2}} = F\left(U^L_{j+\frac{1}{2}}, U^R_{j+\frac{1}{2}}\right)$$

with $U = [Y_i, u, p, T]$.

With the proposed model, two interface fluxes are computed. The first $F^L_{j+\frac{1}{2}} = F\left(U^L_{j+\frac{1}{2}}, U^R_{j+\frac{1}{2}}, W^L_{j+\frac{1}{2}}\right)$ assumes that fluids in both cells $j$ and $j+1$ (i.e. on both sides of the interface) are $W^L$ fluids. The second $F^R_{j+\frac{1}{2}} = F\left(U^L_{j+\frac{1}{2}}, U^R_{j+\frac{1}{2}}, W^R_{j+\frac{1}{2}}\right)$ assumes that fluids in both cells $j$ and $j+1$ are $W^R$ fluids with $W = [\gamma, \rho h_0^m]$. For uniform velocity and pressure, this model affects only the total energy balance, through the internal energy contribution. Mass and momentum are perfectly conserved (essentially conserved if $u$ and $p$ are continuous) (see [11]).

This definition of two fluxes at each interface is equivalent to freeze $\gamma$ and $\rho h_0^m$ on each domain $[j-1/2, j+1/2]\times[n, n+1]$ (for a one time step scheme, we freeze them only on the interval $[j-1/2, j+1/2]$) and to get $W^L_{j+1/2} = W^R_{j-1/2} = W^n_j$. The conserved quantities are computed as:

$$\begin{bmatrix} (\rho Y_i)^{n+1} \\ (\rho u)^{n+1} \\ \rho^{n+1} E^* \end{bmatrix}_j = V_j^n - \frac{\delta t}{\Delta x}\left[F^L(U^L_{j+1/2}, U^R_{j+1/2}, W_j) - F^R(U^L_{j-1/2}, U^R_{j-1/2}, W_j)\right]^n.$$

The thermodynamical quantities are updated in the following step.

*2.2.2. Second step*

From (3), we compute, at mesh point $j$ (subscript df means double flux)

$$p_{\mathrm{df}}^{n+1} = (\gamma_j^n - 1)\left[\rho^{n+1}E^* - (\rho h_0^m)^n - \tfrac{1}{2}(\rho u^2)^{n+1}\right]_j,$$

$$T^{n+1} = \frac{p_{\mathrm{df}}^{n+1}}{\Re \sum_{i=1}^{N} \frac{(\rho Y_i)_j^{n+1}}{M_i}},$$

$$C_{Pi}^{n+1} = C_{Pi}(T^{n+1}), \quad \gamma_{\mathrm{df}}^{n+1} = \gamma(Y_i^{n+1}, C_{Pi}^{n+1}),$$
$$I_m^{n+1} = I_m(T^{n+1}), \quad (h_{i0}^m)^{n+1} = h_{i0}^m(T^{n+1}, T_m^{n+1}),$$

to update

$$(\rho E)^{n+1} = \frac{p_{\mathrm{df}}^{n+1}}{\gamma_{\mathrm{df}}^{n+1} - 1} + (\rho h_0^m)^{n+1} + \frac{(\rho u^2)^{n+1}}{2}.$$

It is essential to follow the order of these steps and sub-steps, otherwise any improvement disappears.

*2.2.3. Remark*

This set of two steps amounts to split time variation of the internal energy $\delta e = e^{n+1} - e^n$ up two parts:

$$\delta e = \delta\left(\frac{p}{(\gamma-1)\rho}\right) = \left(\frac{1}{\gamma-1}\right)^n \delta\left(\frac{p}{\rho}\right) + \left(\frac{p}{\rho}\right)^{n+1} \delta\left(\frac{1}{\gamma-1}\right) = (e^* - e^n) + (e^{n+1} - e^*),$$

where $e^* = E^* - \frac{(u^2)^{n+1}}{2}$. First, the time variation of $e$ is computed with a time frozen $\gamma$. That is equivalent to do a spatial freezing of $\gamma$ on the interval $[j-1/2, j+1/2]$ during the first step since $\gamma$ satisfies [3,11]

$$\delta\left(\frac{1}{\gamma-1}\right) = -\sigma u \Delta\left(\frac{\gamma}{\gamma-1}\right).$$

Then, at the second step, $\frac{p}{\rho}$ is frozen at the time $(n+1)\delta t$ and we compute the time variation of $\frac{1}{\gamma-1}$.

*2.3. Conservation loss*

The conservation loss of the total energy has been quantify from two simulations when $\gamma$ varies ($1.295 \leqslant \gamma \leqslant 1.38$). The first simulation represents the convection of a square wave of $H_2$ in $O_2$. Both interfaces are spread on about ten per cent of the grid mesh. The second case is a sequence of $H_2$ pockets separated by the air. The variations of $\gamma$ concern about 66% of the grid mesh. The error at time $n$

$$\mathrm{Err}(n) = \left| \frac{\sum_{j=1}^{J\max} [W^0 - W^n]}{\sum_{j=1}^{J\max} W^n} \right|,$$

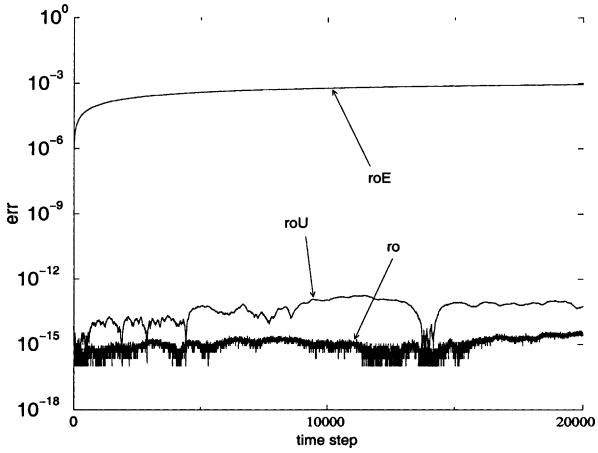


Fig. 1. Conservation loss, variation of $\gamma$ on 10% of the domain.

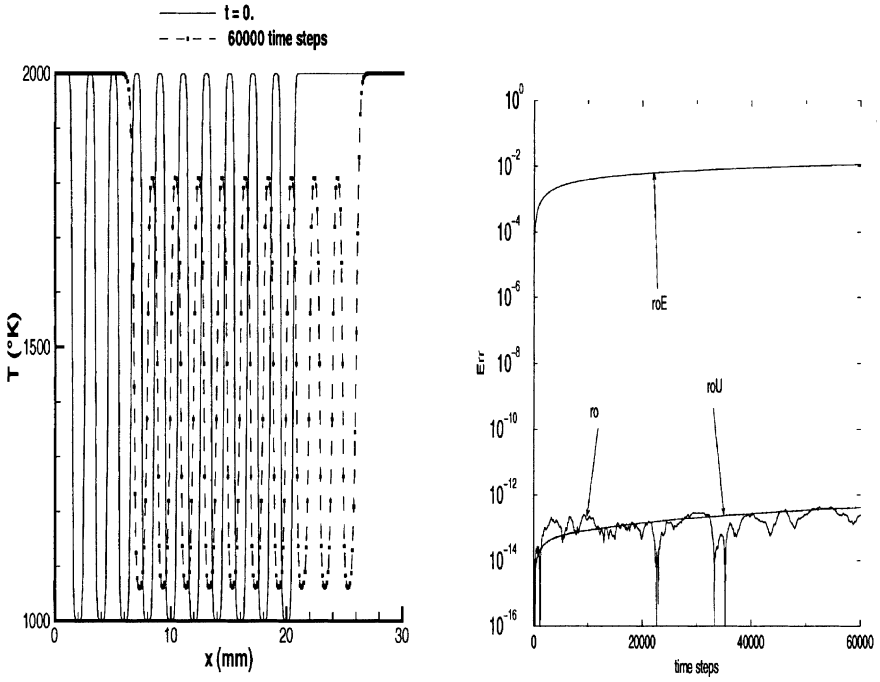


Fig. 2. Left: temperature evolution, right: conservation loss (variation of $\gamma$ on 66% of the domain).

is plotted for $W = [\rho, \rho u, \rho E]^{\mathrm{T}}$. For the lonely wave, the error on the total energy reaches $10^{-3}$ from $n = 20,000\delta t$ (Fig. 1). For the sequence of waves, the error is higher and reaches $10^{-2}$ at $n = 60,000\delta t$ (Fig. 2). In both simulations, the errors on the density and the momentum remain

negligible. We may consider this loss is admissible for a large set of applications even when $\gamma$ varies on a large region of the computational domain.

### 2.4. Multi-time step algorithms

The double flux model may be used with the multi-time step algorithms. The basic idea of the 'double flux model' is the freezing of $W_j^n$ on the space $[j-1/2, j+1/2] \times [n, n+1]$ during the time integration $[n, n+1]$ and its updating only at the end of all the time steps included in $[n, n+1]$. We describe the procedure with a second-order Runge–Kutta algorithm. In order to keep the pressure through the interfaces, it is essential to follow the algorithm in the presented order.

$W_j^n$ is frozen on the space $[j-1/2, j+1/2] \times [n, n+1]$ and the predictor $\widetilde{V}_j$ is computed at time $n+1$:

$$\begin{bmatrix} \widetilde{\rho Y_i} \\ \widetilde{\rho u} \\ \widetilde{\rho E} \end{bmatrix}_j = V_j^n - \frac{\delta t}{\Delta x}\left[F^L(U^L_{j+1/2}, U^R_{j+1/2}, W_j) - F^R(U^L_{j-1/2}, U^R_{j-1/2}, W_j)\right]^n.$$

The quantities $\widetilde{U}$ are updated:

$$\widetilde{Y}_i = \frac{\widetilde{\rho Y_i}}{\sum_{i=1}^N \widetilde{\rho Y_i}},$$

$$\tilde{u} = \frac{\widetilde{\rho u}}{\sum_{i=1}^N \widetilde{\rho Y_i}},$$

$$\tilde{p}_{\mathrm{df}} = (\gamma_j^n - 1)\left[\widetilde{\rho E} - (\rho h_0^m)^n - \tfrac{1}{2}\widetilde{\rho u}\tilde{u}\right]_j,$$

$$\widetilde{T} = \frac{\tilde{p}_{\mathrm{df}}}{\Re \sum_{i=1}^N \frac{\widetilde{\rho Y_i}}{M_i}}.$$

The corrected values are determined from the predicted ones:

$$\begin{bmatrix} (\rho Y_i)^{n+1} \\ (\rho u)^{n+1} \\ (\rho E)^* \end{bmatrix}_j = \frac{V_j^n + \widetilde{V}_j}{2} - \frac{\delta t}{2\Delta x}\left[F^L(\widetilde{U}^L_{j+1/2}, \widetilde{U}^R_{j+1/2}, W_j^n) - F^R(\widetilde{U}^L_{j-1/2}, \widetilde{U}^R_{j-1/2}, W_j^n)\right].$$

$$p_{\mathrm{df}}^{n+1} = (\gamma_j^n - 1)\left[(\rho E)^* - (\rho h_0^m)^n - \tfrac{1}{2}(\rho u^2)^{n+1}\right]_j,$$

$$T^{n+1} = \frac{p_{\mathrm{df}}^{n+1}}{\Re \sum_{i=1}^N \frac{(\rho Y_i)_j^{n+1}}{M_i}},$$

$$C_{Pi}^{n+1} = C_{Pi}(T^{n+1}), \quad \gamma_{\mathrm{df}}^{n+1} = \gamma(Y_i^{n+1}, C_{Pi}^{n+1}),$$
$$I_m^{n+1} = I_m(T^{n+1}), \quad (h_{i_0}^m)^{n+1} = h_{i_0}^m(T^{n+1}, T_m^{n+1}),$$

to update

$$(\rho E)^{n+1} = \frac{p_{\mathrm{df}}^{n+1}}{\gamma_{\mathrm{df}}^{n+1} - 1} + (\rho h_0^m)^{n+1} + \frac{(\rho u^2)^{n+1}}{2}.$$

### 2.5. Limiters

With the MUSCL approach [14], the backward and forward extrapolated values of $U_{j+\frac{1}{2}}$ can be written as:

$$U_{j+1/2}^L = L(U_{j-1}, U_j, U_{j+1}) = U_j + \frac{\varphi(r_j)}{2}(U_{j+1} - U_j),$$

$$U_{j+1/2}^R = R(U_j, U_{j+1}, U_{j+2}) = U_{j+1} - \frac{\varphi\left(\frac{1}{r_{j+1}}\right)}{2}(U_{j+1} - U_j).$$

Here, $r_j = \frac{U_j - U_{j-1}}{U_{j+1} - U_j}$ is the slope ratio of the quantity $U$ at node $j$. Optimal expressions of $\varphi$ have been defined. They depend on the characteristics of the flow in order to keep good properties of the accuracy and stability of the numerical scheme.

When velocity and pressure fluctuations exist in a flow field (turbulent flow for instance), the flux splitting is activated and we have associated with it a triad of limiters $\varphi_{\mathrm{triad}}$, each adapted to the local variation of the physical quantities [1,2]. If the variation is monotone in interval $[j-2, j+2]$, the expression at the node $j$ is

$$\varphi_{\mathrm{triad}} = \frac{1}{2}\left[(1-\kappa)\min\left(r, \frac{3-\kappa}{1-\kappa}\right) + (1+\kappa)\min\left(1, \frac{(3-\kappa)r}{1-\kappa}\right)\right] \quad \text{with} \quad \kappa = 1/3.$$

When $r_j \leqslant 0$ or when $r_j > 0$ and wave number $k$ associated with the physical fluctuation verifies $k = \frac{2\pi}{3\Delta x}$ or $k = \frac{\pi}{\Delta x}$, we get

$$\varphi_{\mathrm{triad}} = 0.$$

For the other cases, we choose the least dissipative limiter in order to develop the energy cascade

$$\varphi_{\mathrm{triad}} = 1.$$

That corresponds to a centered interpolation of $U$. This set of limiters is coupled with the AUSM$^+$ splitting [15] whose the dissipative properties balance well the compressive effects of the triad.

But when a flow has a constant pressure and a constant velocity, the AUSM$^+$ splitting is not called and the scheme becomes too compressive with the triad. It is advantageous to associate the extrapolations with only one limiter MinMod, less compressive than the triad, in a MUSCL procedure:

$$\varphi_d = \tfrac{1}{2}[(1-\kappa)\min(r, \omega) + (1+\kappa)\min(1, \omega r)]$$

with $\kappa = 1/3$ and $1 \leqslant \omega \leqslant 4$.

In practice, we adapt the limiter expression to the flow field (adaptive limiters). We use a switch that allows to apply $\varphi_d$ when the pressure fluctuations are weak ($\Delta p/p \leqslant \varepsilon$). We have chosen arbitrary $\varepsilon = 0.001$. The $\varphi_{\mathrm{triad}}$ is activated anywhere else only through the shocks where the first-

order AUSM$^+$ scheme ($\varphi = 0$) is applied so for avoiding the overshoot and the spurious oscillations behind the shock.

### 2.6. Navier–Stokes equations

This algorithm written for the Euler equations is introduced in a code which solves the Navier–Stokes equations. If we assume

- the Lewis numbers are equal ($Le_i = Le$),
- the diffusion velocity is represented by the Fick's law,
- the Stokes' hypothesis is valid,
- the thermal conductivity $\lambda = \frac{\bar{\mu} C_P}{Pr}$,

the 1-D Navier–Stokes equations are written

$$V_i + f_x = S \quad \text{with}$$

$$V = \begin{bmatrix} \rho Y_i \\ \rho u \\ \rho E \end{bmatrix}, \quad f = \begin{bmatrix} \rho u Y_i - \frac{\bar{\mu}}{PrLe} \frac{\partial Y_i}{\partial x} \\ \rho u^2 + p - \frac{4}{3} \bar{\mu} \frac{\partial u}{\partial x} \\ \rho u H - \frac{4}{3} \bar{\mu} u \frac{\partial u}{\partial x} - \frac{\bar{\mu} C_P}{Pr} \frac{\partial T}{\partial x} - \frac{\bar{\mu}}{PrLe} \sum_{i=1}^{N} h_i \frac{\partial Y_i}{\partial x} \end{bmatrix}, \quad S = \begin{bmatrix} \overset{\circ}{W}_i \\ 0 \\ 0 \end{bmatrix}.$$

$Pr$ is the Prandtl number of the mixture. Its value is fixed to 0.4 and $Le = 1$. The viscosity of the mixture is expressed

$$\bar{\mu} = \frac{1}{2} \left[ \sum_{i=1}^{N} X_i \mu_i + \left( \sum_{i=1}^{N} \frac{X_i}{\mu_i} \right)^{-1} \right],$$

where $\mu_i$ is the viscosity of the pure component $i$ and $X_i = \frac{\frac{Y_i}{M_i}}{\sum_{j=1}^{N} \frac{Y_j}{M_j}}$. The viscosity $\mu_i$ is obtained by a fourth-order polynomial in $T$. All the viscous and diffusion terms are solved with a centered second-order scheme in space. The simulations have been performed with the one-time step and the two-time step schemes and with the same CFL. The results obtained being quasi-identical, only the results obtained with the single time step scheme are presented.

## 3. 1-D numerical examples

### 3.1. 1-D convection of an inert front $H_2$–$O_2$

For this first case, the Euler equations are solved. The front $H_2$–$O_2$ is convected with a constant velocity $u = 20$ m/s in a uniform pressure field $p = 10^5$ Pa. At $t = 0$, the front thickness is 0.7 mm. $T_{H_2} = 1000$ K and $T_{O_2} = 2000$ K. The run parameters are set as: CFL = 0.5, $\omega = 1.5$. The grid mesh $\Delta x = 0.1$ mm and the time step is $\delta t \approx 2 \times 10^{-8}$ s. We compare the numerical and exact solutions of the hydrogen mass fraction at $t = 4 \times 10^{-4}$ s (Fig. 3a). The front is convected with the correct velocity and remains smooth. The numerical diffusion is weak. To have a better

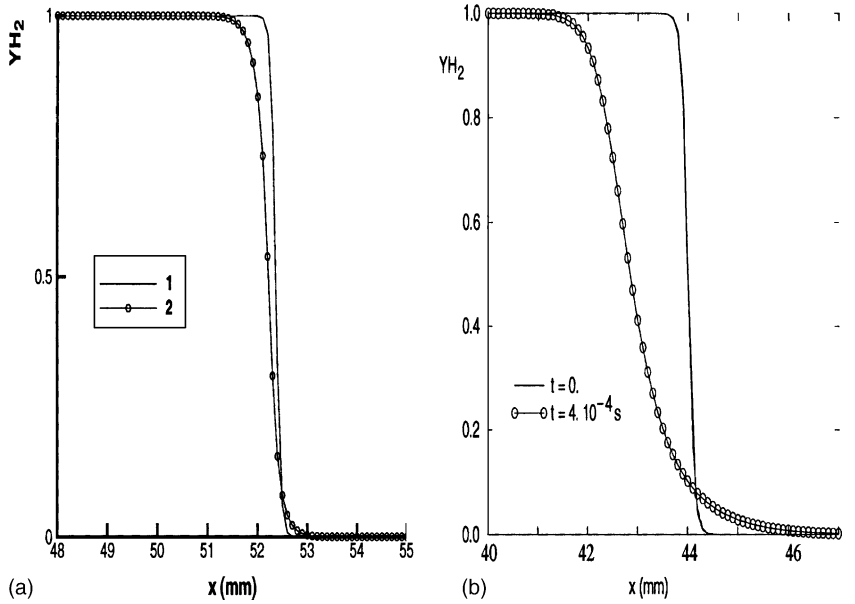


Fig. 3. 1-D convection of an inert front; mass fraction of hydrogen, (a) exact solution (1) and numerical solution (2) at $t = 4 \times 10^{-4}$ s (20,000 time steps), (b) DNS solution at $t = 0$ and at $t = 4 \times 10^{-4}$ s.

quantitative information about the numerical diffusion, we have used a DNS code [13] on this case with the same grid mesh and time step and with the same initial solution, excepted for the velocity, here equal to zero (Fig. 3b). The direct numerical simulation is performed with nonunity Lewis numbers and the Soret effect are taken into account. A sixth-order-accurate in space and a fourth-order-accurate in time schemes are used. This computation allows to compare the numerical diffusion of the mass fractions and the temperature of our approach (Figs. 3a and 4a), with the mass and thermal diffusions of the front at the same time (Figs. 3b and 4b). The physical diffusions have spread the front on about 6 mm for the species and the temperature while the numerical diffusion has spread them on 1.5 mm. The numerical diffusion of the proposed algorithm is clearly weaker than the physical diffusions. This conclusion is also verified when the molecular weights are close to each other ($O_2$ and $N_2$ for example) and for very different velocities (this case has been performed with 0.5 m/s $\leqslant u \leqslant$ 1800 m/s). A weak lagging of the computed solution appears when the molecular weights ratio is high (Figs. 3a and 4a). The pressure (Fig. 5) and velocity remain rigorously constant during the time integration. The evolutions of $C_p$ and the density are also presented in Fig. 5.

### 3.2. 1-D convection–diffusion of reactive fronts $H_2$–$O_2$

The initial values are the same than ones in the previous case but the profiles of mass fraction $Y_{H_2}$ and the temperature are defined as

$$Y_{H_2} = \frac{1}{2}\left[1 + \tanh\left(C_r\left(\frac{l}{2} - |x - x_0|\right)\right)\right], \quad T = 1500\left[1 - \frac{1}{3}\tanh\left(C_r\left(\frac{l}{2} - |x - x_0|\right)\right)\right]$$

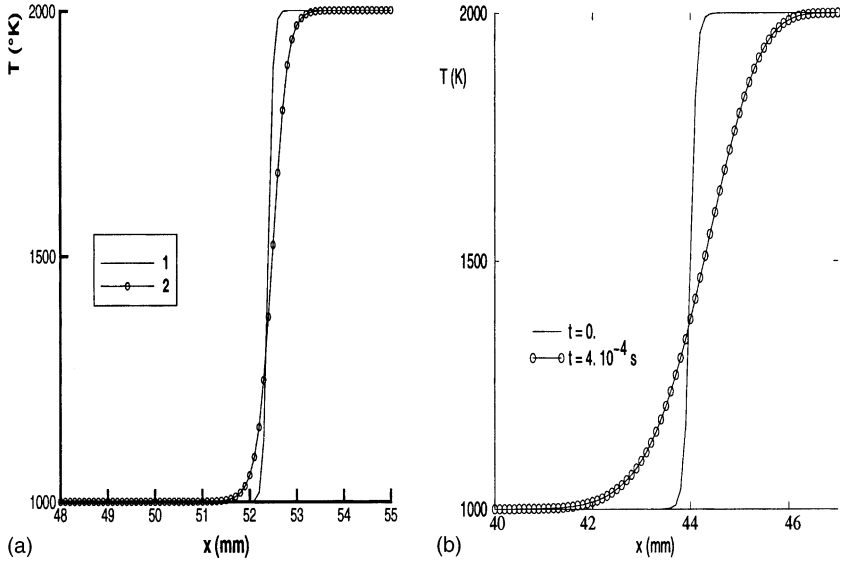


Fig. 4. 1-D convection of an inert front; temperature, (a) exact solution (1) and numerical solution (2) at $t = 4 \times 10^{-4}$ s (20,000 time steps), (b) DNS solution at $t = 0$ and at $t = 4 \times 10^{-4}$ s.

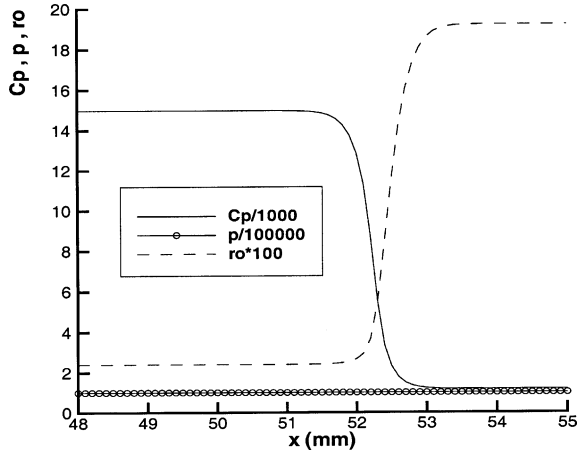


Fig. 5. 1-D convection of an inert front; constant-pressure specific heat, pressure and density at $t = 4 \times 10^{-4}$ s.

in order to have two symmetric fronts. This configuration allows to verify if the upwind schemes, used to solve the hyperbolic part, keep the symmetry of the problem during the time evolution. At $t = 0$, the center of the plateau $x_0 = 20$ mm and its length $l = 6$ mm with parameter $C_r = 80$. The Rogers–Chinitz model is applied [12]. This model was developed to represent $H_2$–*air* combustion kinetics with as few reaction steps and species as possible. It consists of the following two steps:

$$H_2 + O_2 \leftrightarrow 2OH$$

$$2OH + H_2 \leftrightarrow 2H_2O$$

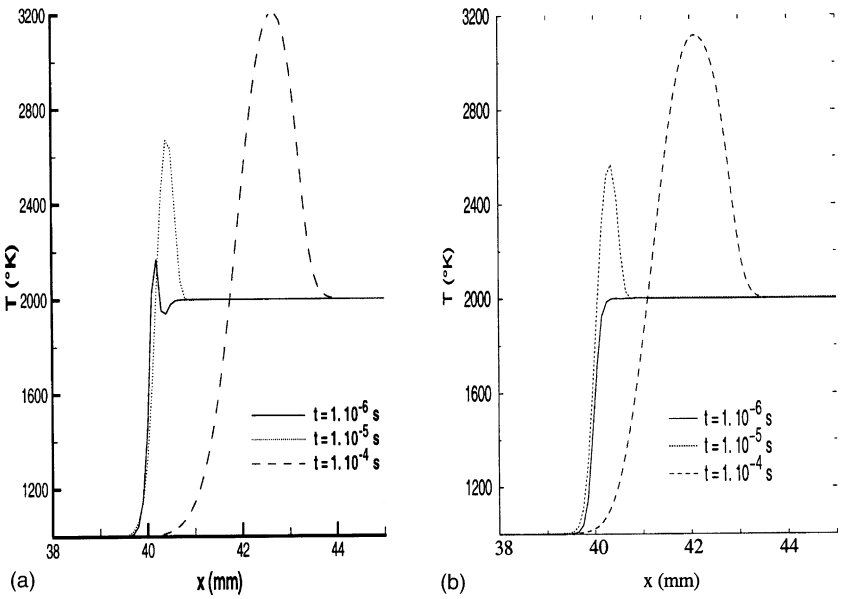


Fig. 6. 1-D convection of reactive front $H_2$–$O_2$ (a) solution with the double flux and Rogers–Chinitz model, (b) solution with the DNS code and detailed chemical model.

In this study, the first reaction step is assumed to be in a chemical equilibrium. In order to compare with the DNS results, the diffusion and viscous terms are taken into account. In Fig. 6, the evolution of the temperature on the right front, obtained with the Rogers–Chinitz model, is compared to the result obtained with the DNS code and a detailed chemistry model (9 species and 38 reactions). With the Rogers–Chinitz model, the ignition occurs earlier because the first reaction step. The maximum value of $T$ is well described during the time evolution but its location is not exactly at the correct place ($x_{T_{\max}} = 42.7$ mm and $x_{T_{\max}} = 42.1$ mm for the DNS computation). The flame thickness is slightly thinner (3.8 mm at $t = 10^{-4}$ s instead of 4 mm for the DNS result).

The profiles of mass fractions $Y_{H_2}$, $Y_{O_2}$ and $Y_{H_2O}$, the temperature and the pressure are presented at $t = 10^{-4}$ s in Fig. 7a. Even with a stiff source term, the pressure, and then the velocity, are perfectly preserved with the proposed method and the symmetry of the flow is well-preserved.

With a pure conservative method, the solution presents (Fig. 7b), very quickly (here, at time $t = 8 \times 10^{-6}$ s), oscillations on the pressure, temperature but more particularly on the velocity. At the initial time, $u = 20$ m/s and at $t = 8 \times 10^{-6}$ s we have already $-340$ m/s $\leqslant u \leqslant 480$ m/s and the maximum value of the temperature is too high. Therefore, the nonuniform evolution of $p$ in a contact discontinuity may generate a bad description of the chemical process (see also some test cases in [11]).

## 4. Extension to 2-D reactive flows

A time-splitting method is used. The 2-D finite difference operator is split into a product of simpler operators:

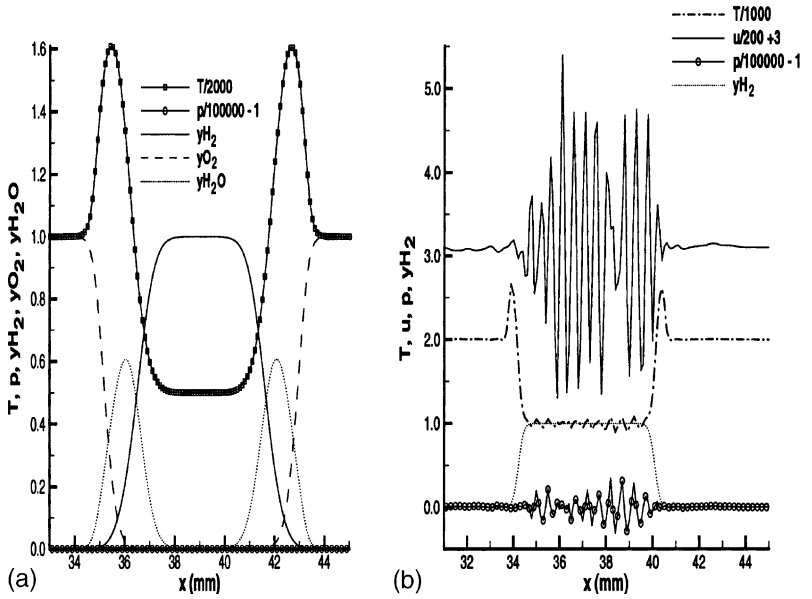


Fig. 7. 1-D convection of reactive fronts, (a) solution with the double flux model at $t = 10^{-4}$ s, (b) solution with the classical conservative scheme at $t = 8 \times 10^{-6}$ s.

$$V_j^{n+2} = \left( \mathscr{L}_{H_x}\left(\frac{\delta t}{6}\right) \mathscr{L}_{H_y}\left(\frac{\delta t}{6}\right) \mathscr{L}_{P_{xy}}\left(\frac{\delta t}{3}\right) \mathscr{L}_{s}\left(\frac{2\delta t}{3}\right) \mathscr{L}_{P_{xy}}\left(\frac{\delta t}{3}\right) \mathscr{L}_{H_y}\left(\frac{\delta t}{6}\right) \mathscr{L}_{H_x}\left(\frac{\delta t}{6}\right) \right) V_j^n, \quad (5)$$

where $\mathscr{L}_{H_x}$ and $\mathscr{L}_{H_y}$ are the operators associated with the hyperbolic terms in $x$- and $y$-directions, $\mathscr{L}_{P_{xy}}$ is the operator associated with the parabolic terms and $\mathscr{L}_s$ is the operator that solves the source terms of the Navier–Stokes equations.

### 4.1. Convection–diffusion of a circular flame

The last case is extended to 2-D flows. The spot of hydrogen has now a top-hat shape, $Y_{H_2} = \frac{1}{2}(1 + \tanh(C_r(\frac{l}{2} - |r - r_0|)))$ with always $C_r = 80$ and $l = 6$ mm, $r$ is the spot radius and $r_0$ its center ($x_0 = 5$ mm, $y_0 = 15$ mm). The run parameters are $\Delta x = \Delta y = 0.1$ mm, CFL $= 0.5$, $\omega = 1.5$. In order to avoid a too particular study (convection along an axis or a diagonal line for example), the spot is convected with angle $\beta = -18°$ with the axis $x$. The velocity components are $u = 78$ m/s, $v = -25$ m/s. The computational domain $(x, y)$ has a dimension 40 mm by 20 mm. The boundary conditions are periodic in both directions. If we plot the distribution of the temperature at $t = 1.6 \times 10^{-4}$ s (Fig. 8), we observe the circular shape is well preserved during the convection. As in 1-D simulations, the pressure and velocity are perfectly conserved. We have also plotted, at the same time, the position of the spot of temperature if it had been advected only (thick contours). The exact and computed contours are perfectly concentric. Therefore, the model, proposed here, may be extended to the multi-dimensional problems.

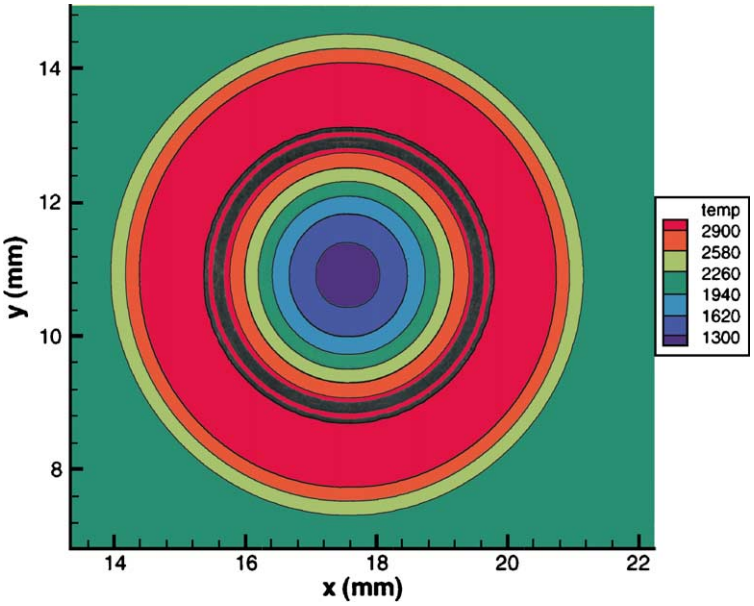


Fig. 8. 2-D convection of a circular $H_2$–$O_2$ front, temperature at $t = 1.6 \times 10^{-4}$ s (8000 time steps), thick contours: advection only.

### 4.2. Interaction vortices-reactive fronts $H_2$–$O_2$–$N_2$

#### 4.2.1. Initial conditions

In order to verify if the model proposed here is valid also for flows with strong variations of the pressure, we study the interaction of a spot of temperature moving in a supersonic flow with a steady shock. The gas is composed with air excepted in a zone, that runs alongside the shock, filled in with $H_2/N_2$ ($Y_{H_2} = 0.233$). This interaction sets up two counter-rotating vortices that are going to stretch both fronts $H_2/N_2$–*air*. The interaction of an isolated cylindrical gas inhomogeneity with a shock has been studied experimentally and numerically by some laboratories ([17–21] for example). We have added, just behind the shock, two diffusion zones. The interest of this problem is the study of the action of a vortex pair, with an inner high temperature, on the quenching of a gaseous front when the chemical reactions appear simultaneously with this interaction or have already started or are completely developed. In this paper, we simulate the case where the vortex pair stretches the fronts at the beginning of reactions.

The dimensions of the domain $(x, y)$ are 30 mm × 10 mm. The inlet flow conditions are $T = 400$ K, Mach number $M = 2.5$, $p = 10^5$ Pa. The $y$-component of the velocity is equal to zero. The simulation is run on a fine grid ($\Delta x = \Delta y = 25$ μm). The thickness of all the fronts (circular and straight fronts) are about 0.25 mm (ten cells). The shock is represented on one cell. The value of the inlet Reynolds number calculated on the diameter of the spot is 50,000, time step $\delta t = 6 \times 10^{-9}$ s and CFL = 0.5. The temperature in the spot is 2000 K and about 400 K in the $H_2/N_2$ zone. The pressure and velocity in front of and behind the shock are constant at $t = 0$. Periodic conditions are applied on the upper and lower boundaries. The spatial distribution of the temperature just before the interaction spot-shock is presented in Fig. 9.

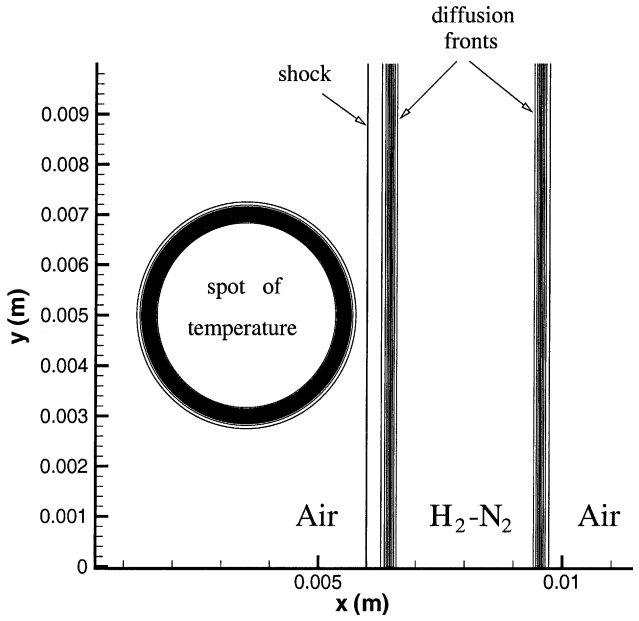


Fig. 9. Interaction vortex-reactive fronts, temperature field just before the hit.

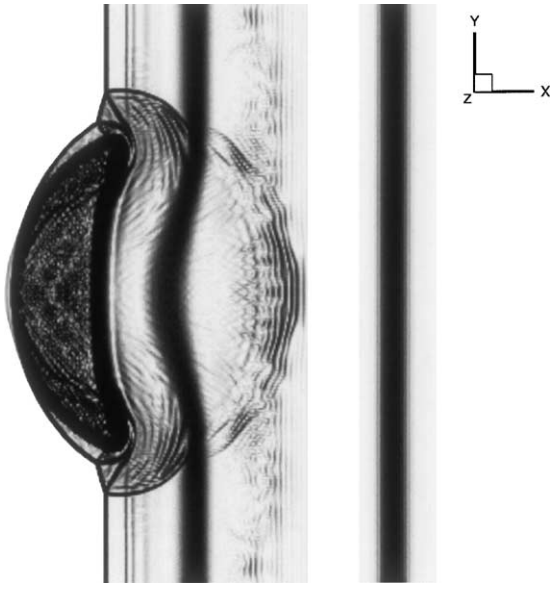


Fig. 10. Temperature field at $t = 3.3 \times 10^{-6}$ s.

*4.2.2. Results*

The temperature field may be visualized during the interaction spot-shock in Figs. 10 and 11. At $t = 3.3 \times 10^{-6}$ s after the hit, the 2-D shade numerical image shows clearly the four shock

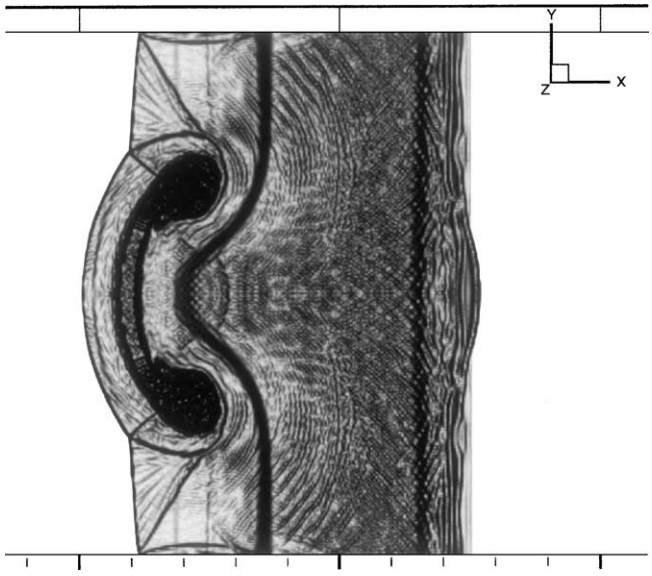


Fig. 11. Temperature field at $t = 7 \times 10^{-6}$ s.

configuration formed that Henderson et al. [19] have called twin regular reflection–refraction (TRR). The expansion fan is visible and its shape changes through the diffusion zone because the mixing $H_2/N_2$ has a higher sound speed than the surrounding air. The vertical lines ahead of the concentric waves come from the initialization of the computation. At $t = 0$, since $\gamma$ is assumed to vary through the shock, it is not possible to find directly the upstream values from the downstream ones. The jump conditions through the shock are calculated from a Newton method and without taking account to the viscous effects. At the beginning of the simulation, weak oscillations in the normal direction of the shock set up, mainly due to the activation of the viscous terms which are absent at the initialization of the flow field.

At $t = 7 \times 10^{-6}$ s, the vortices generated at the edge of the bubble appear and induce a jet of air along the axis of flow symmetry. The first diffusion zone is breathed between the vortex pair. The concentric acoustic waves issue to the oscillations of the skin of the bubble are visible and develop a complex acoustic system. The algorithm produces very thin shocks (spread at the most on two cells) even when they are not aligned with the mesh. The contact discontinuities emanating from the triple points are well represented too.

The view on Fig. 12 at the same time allows to verify the absence of overshoot and undershoot near the shock and to observe the very stiff phenomena captured by this method.

A blow-up view of the temperature in the interaction region shows, at different times ($t = 1.5 \times 10^{-6}$ s, $3.5 \times 10^{-6}$ s and $7 \times 10^{-6}$ s), the set up of an instability of the skin of the bubble that appears gradually (Figs. 13–15). These plots all use forty equally spaced contours between 400 and 3000 K. At the end, a pocket of lower temperature is separated of the core of the bubble. Inside the bubble, a complex acoustic waves system appears (Fig. 14) which becomes organized at $t = 7 \times 10^{-6}$ s. The waves take the same direction and seem to be in phase with the instabilities of the skin of the bubble (Fig. 15). These flow characteristics look like the phenomena in Hass and

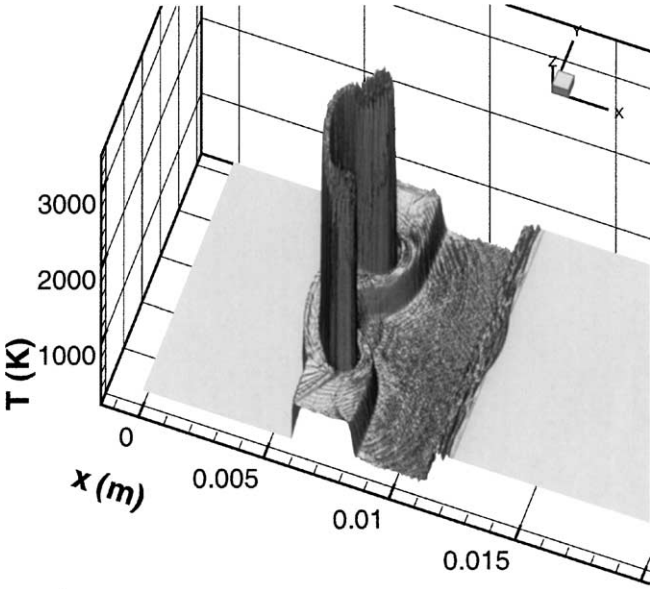


Fig. 12. Temperature field at $t = 7 \times 10^{-6}$ s.

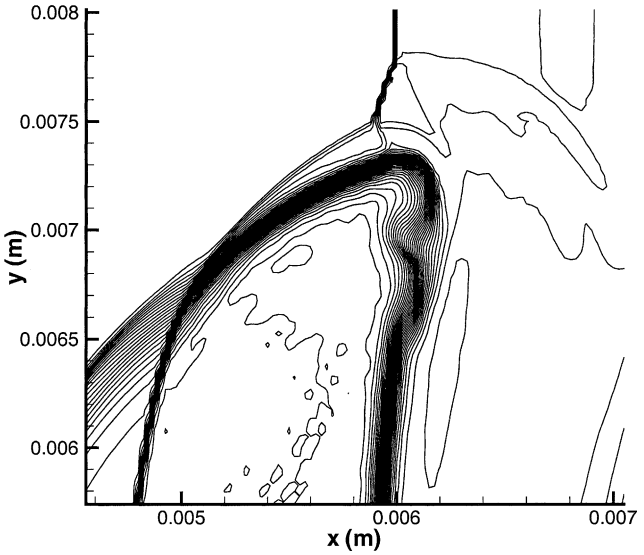


Fig. 13. Blow-up of the temperature field at $t = 1.5 \times 10^{-6}$ s.

Sturtevant's experiment [17] and Quirk and Karni's simulation [20] where instabilities appear inside the bubble and where the interface becomes instable after the interaction.

The same simulation has been performed with limiter $\varphi_d$ with $\omega = 1$ (MinMod limiter). It represents the lower limit of the second-order TVD domain and is considered as the more diffusive

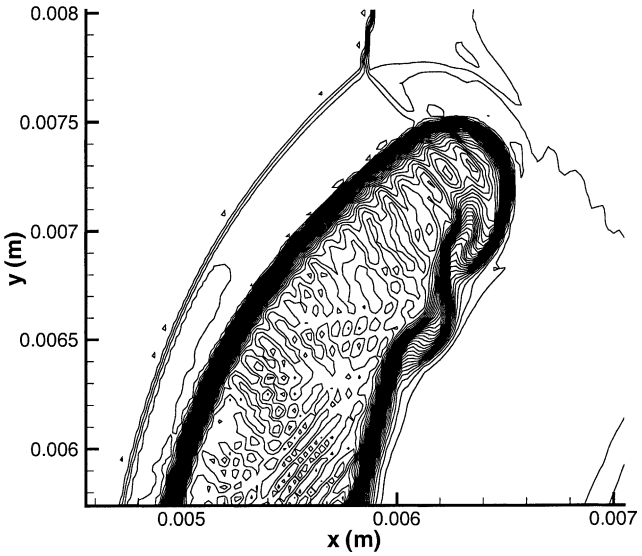


Fig. 14. Blow-up of the temperature field at $t = 3.5 \times 10^{-6}$ s.

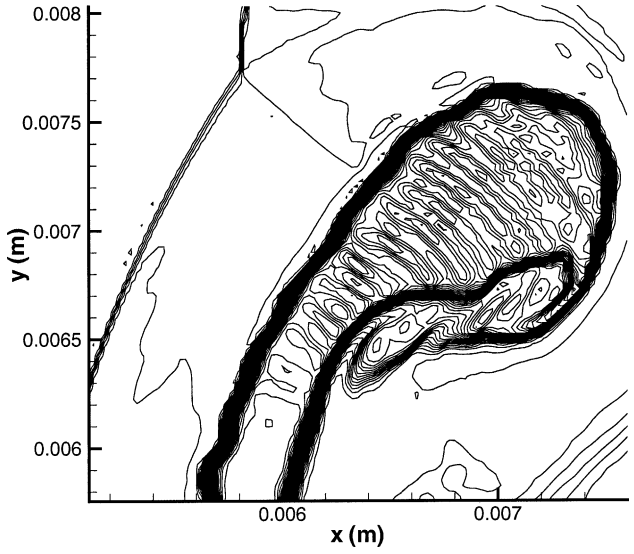


Fig. 15. Blow-up of the temperature field at $t = 7 \times 10^{-6}$ s.

limiter. The temperature field is presented at $t = 7 \times 10^{-6}$ s. The comparison of Figs. 11 and 16 shows the main features of the flow are present in both simulations but they are clearly more accentuated with the triad which keeps better the amplitude of the fluctuations as shown in [1,2]. The contact discontinuities, the skin of the bubble and the diffusion zones remain thinner with the triad while the numerical diffusion of the MinMod limiter acts rapidly. Particularly, if we compare Figs. 15 and 17 where the region of the bubble is plotted, we observe the same fluctuations but

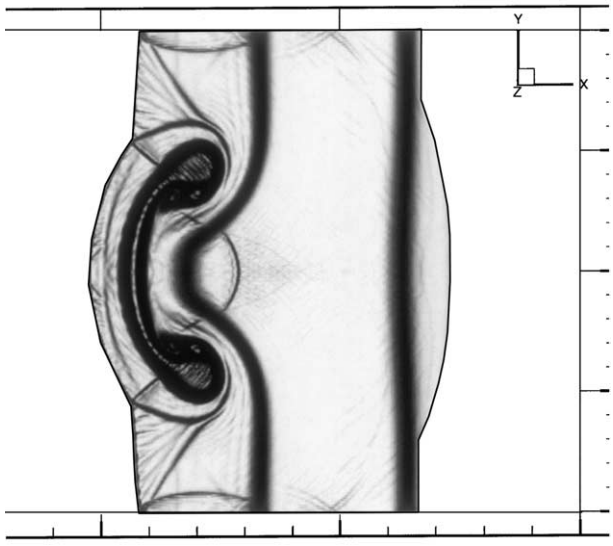


Fig. 16. Temperature field at $t = 7 \times 10^{-6}$ s, MinMod limiter.

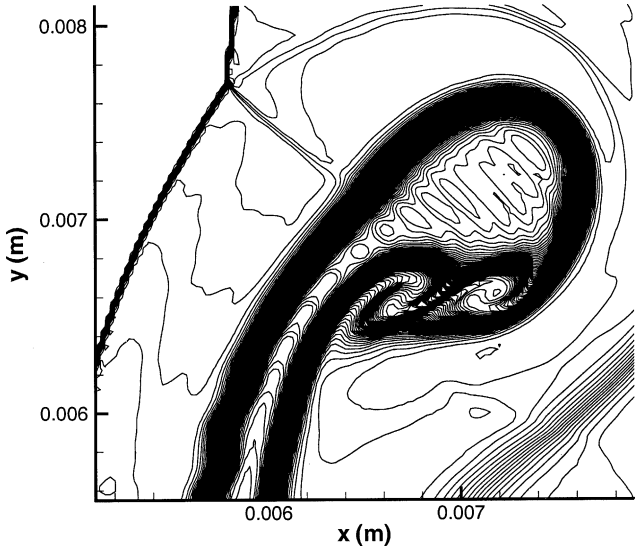


Fig. 17. Blow-up of the temperature field at $t = 7 \times 10^{-6}$ s, MinMod limiter.

their amplitudes are much less attenuated with the triad than the MinMod limiter (so for visualizing the waves in Fig. 17, the plots use 120 equally spaced contours between 400 and 3300 K instead of 40 in Fig. 15).

The instability, which begins to appear along the first contact discontinuity in Fig. 11, is still apparent in Fig. 18 (CD1). The second contact discontinuity (CD2) which is crossed by the incident shock (S1) coming from the neighboring interaction spot-shock is also instable and develops the

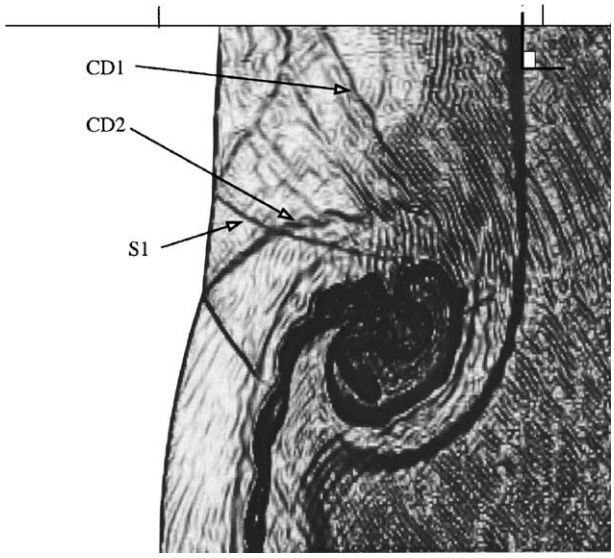


Fig. 18. Blow-up of the temperature field at $t = 1.2 \times 10^{-5}$ s.

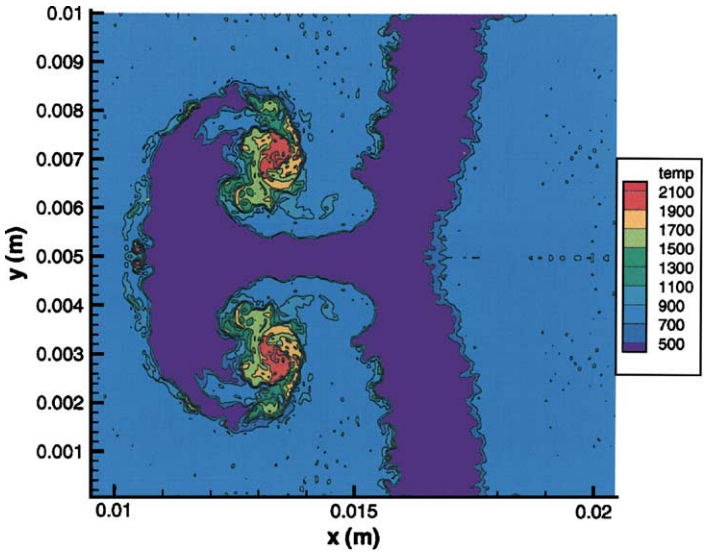


Fig. 19. Blow-up of the temperature field at $t = 2.7 \times 10^{-5}$ s.

Kelvin–Helmholtz rolls. As in [21], a 'mushroom' shape roll up of the cold flow can be seen, related to the Rayleigh–Taylor instability.

The vortex pair influence on the diffusion zones is represented in Fig. 19, at $t = 2.7 \times 10^{-5}$ s. The characteristic mushroom shape is visible but the acoustic waves system developed previously has strongly distorted the first diffusion zone. At $t = 3.7 \times 10^{-5}$ s, the mass fraction of the hy-

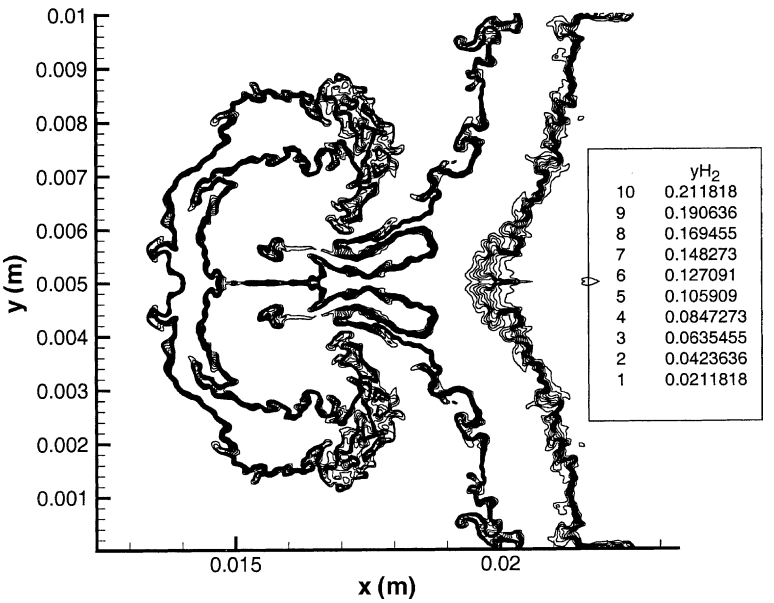


Fig. 20. $Y_{H_2}$ at $t = 3.7 \times 10^{-5}$ s.

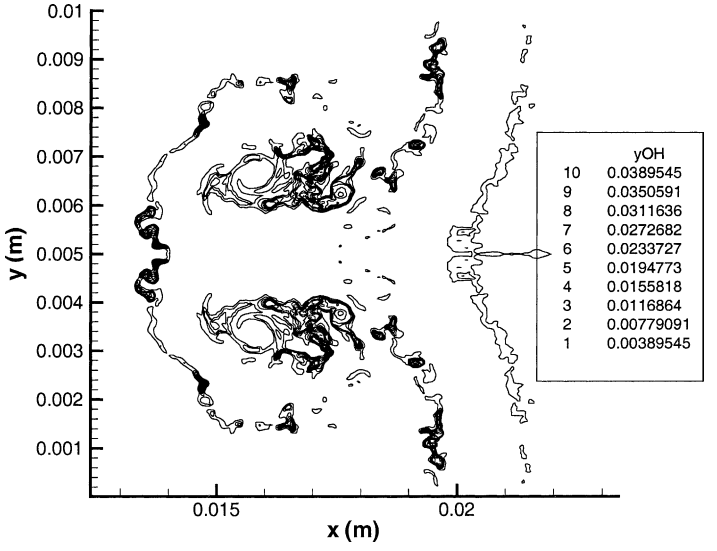


Fig. 21. $Y_{OH}$ at $t = 3.7 \times 10^{-5}$ s.

drogen is plotted in Fig. 20 and shows the strong effect of the velocity field on the stretching of the diffusion zones. The diffusion of the hydrogen is visible mainly ahead of the vortices. Everywhere else, the stretching of the front prevents an effective diffusion of it. The distributions of the mass fractions of $Y_{OH}$ and $Y_{H_2O}$ are drawn on Figs. 21 and 22. We notice the strong oscillations of the

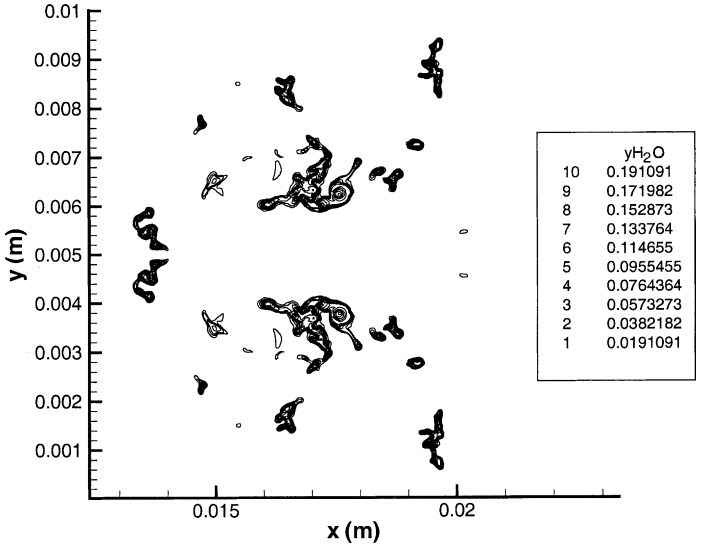


Fig. 22. $Y_{H_2O}$ at $t = 3.7 \times 10^{-5}$ s.

flame surface area resulting from the competition between turbulent wrinkling and flame surface consumption. The main production of $Y_{OH}$ and $Y_{H_2O}$ remains located between the vortices and the symmetry axis.

## 5. Conclusion

The 'double flux model' is extended to the unsteady reactive flows, with $C_{Pi} = C_{Pi}(T)$. This approach associated with a shock-capturing technique allows to solve correctly the gaseous fronts on very large ranges of the speed and the density ratio. This approach may be applied on reactive flows where stiff phenomena exist (strong gradients of temperature, pressure and density). It keeps a good accuracy associated with a good stability. This approach uses simple algorithms (MUSCL approach and one time step) and is cheap compared with the algorithms using high-order schemes in DNS code, for example. Its numerical diffusion is weaker than the mass and thermal diffusions.

The aim is now to extend this approach with more detailed chemical kinetics. With the intrinsic qualities of this approach (good stability, correct accuracy and cheap computational costs), it might be possible to realize 3-D simulations of unsteady reactive flows in a near future.

## References

[1] Billet G, Louédin O. In: A simple algorithm to improve the accuracy of TVD-MUSCL schemes, Hyperbolic Problems: Theory, Numerics, Applications. Int Series Numerical Mathematics, 129. Basel, Switzerland: Birkhauser Verlag; 1999. p. 65–75.

[2] Billet G, Louédin O. Adaptive limiters to improve the accuracy of MUSCL approach for unsteady flows. J Comput Phys 2001;170:161–83.

[3] Abgrall R. Generalization of the Roe scheme for the computation of mixture of perfect gases. Rech Aérosp 1988;6.
[4] Larouturou B, Fezoui L. On the equations of multicomponent perfect or real gas inviscid flow. In: Nonlinear hyperbolic problems, vol. 1402. Heidelberg: Springer-Verlag; 1989. p. 69–97.
[5] Larouturou B. How to preserve the mass fraction positive when computing compressible multi-component flows. J Comput Phys 1991;95:59–84.
[6] Mulder W, Osher S, Sethian J. Computing interface motion: the compressible Rayleigh–Taylor and Kelvin–Helmholtz instabilities. J Comput Phys 1996;100:209.
[7] Fedkiw R, Aslam T, Merriman B, Osher S. A non-oscillatory Eulerian approach to interfaces in multimaterial flows (the ghost fluid method). J Comput Phys 1999;152:457–92.
[8] Jenny P, Muller B, Thomann H. Correction of conservative Euler solvers for gas mixtures. J Comput Phys 1997;132:91–107.
[9] Karni S. Multi-component flow calculation by a consistent primitive algorithm. J Comput Phys 1994;112:31–43.
[10] Abgrall R. How to prevent pressure oscillations in multicomponent flow calculations: a quasi conservative approach. J Comput Phys 1996;125:150–60.
[11] Abgrall R, Karni S. Compressible multifluids. J Comput Phys 2001;169:594–623.
[12] Rogers RC, Chinitz W. On the use of a global hydrogen–air combustion model in the calculation of turbulent reacting flows. AIAA paper 82-0112, 1982.
[13] Thévenin D, Behrendt F, Mass U, Przywara B, Warnatz J. Development of a portable parallel direct simulation code to investigate reactive flows. Comput Fluids 1996;25(5):485–96.
[14] van Leer B. Towards the ultimate conservative difference scheme, V. A second-order sequel to Godunov's method. J Comput Phys 1979;32:101.
[15] Liou MS. A sequel to AUSM: AUSM$^+$. J Comput Phys 1996;129:364.
[16] Liou MS. Ten years in the making—AUSM-family, AIAA 2001-2521. 15th AIAA Computational Fluid Dynamics Conf., June 2001, Anaheim, CA.
[17] Hass JF, Sturtevant B. Interaction of weak shock waves with cylindrical and spherical gas inhomogeneities. J Fluid Mech 1987;181:41–76.
[18] Picone JM, Boris JP. Vorticity generation by shock propagation through bubbles in a gas. J Fluid Mech 1988;189:23–51.
[19] Henderson LF, Colella P, Puckett EG. On the refraction of shock waves at a slow–fast gas interface. J Fluid Mech 1991;224:1–27.
[20] Quirk JJ, Karni S. On the dynamics of a shock–bubble interaction. ICASE report no 94-75, 1994.
[21] Don WS, Quillen CB. Numerical simulation of shock–cylinder interactions. J Comput Phys 1995;122:244–65.